

Vibronic Characteristics and Spin-Density Distributions in Bacteriochlorins as Revealed by Spectroscopic Studies of 16 Isotopologues. Implications for Energy- and Electron-Transfer in Natural Photosynthesis and Artificial Solar-Energy Conversion

James R. Diers,[†] Qun Tang,[†] Christopher J. Hondros,[†] Chih-Yuan Chen,[‡] Dewey Holten,^{*,§} Jonathan S. Lindsey,^{*,‡} and David F. Bocian^{*,†}

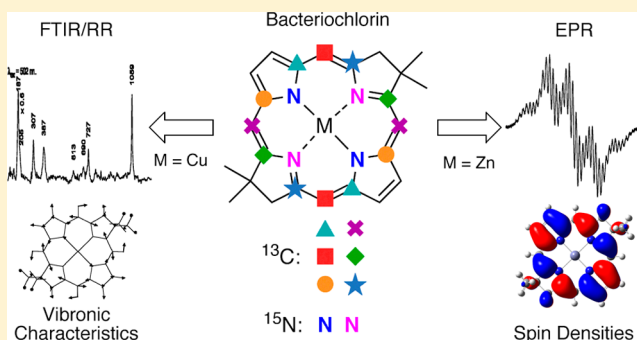
[†]Department of Chemistry, University of California, Riverside, California 92521-0403, United States

[‡]Department of Chemistry, North Carolina State University, Raleigh, North Carolina 27695-8204, United States

[§]Department of Chemistry, Washington University, St. Louis, Missouri 63130-4889, United States

S Supporting Information

ABSTRACT: Vibronic characteristics and spin-density distributions in the core bacteriochlorin macrocycle were revealed by spectroscopic and theoretical studies of 16 isotopologues. The vibrational modes in copper bacteriochlorin isotopologues were examined via resonance Raman and Fourier-transform infrared spectroscopy. The resonance Raman spectra exhibit an exceptional sparsity of vibronically active modes of the core macrocycle, in contrast with the rich spectra of the natural bacteriochlorophylls. The Q_y -excitation resonance Raman spectrum is dominated by a single mode at 727 cm^{-1} , which calculations suggest is due to a symmetrical accordion-like deformation of the five-atom $C_m(C_aNC_a)_{\text{pyrrole}}C_m$ portion of the ring core. This deformation also dominates the vibronic features in the absorption and fluorescence spectra. The spin-density distributions in the π -cation radical of the zinc bacteriochlorin isotopologues were studied by electron paramagnetic resonance spectroscopy. The spectra indicate a significant electron/spin density ($\rho \sim 0.1$) on each *meso*-carbon atom. This observation contradicts the predictions of early calculations that have been assumed to be correct for nearly four decades. Collectively, these findings have implications for how the structural features that characterize natural bacteriochlorophylls might influence energy- and electron-transfer processes in photosynthesis and alter the thinking on the design of synthetic, bacteriochlorin-based arrays for solar-energy conversion.



I. INTRODUCTION

Understanding the physical properties of photosynthetic pigments enables deep insight into the workings of the photosynthetic machinery and is essential for the rational design of bioinspired solar energy conversion systems. Studies of chlorophylls have been a mainstay of photosynthesis research, not surprisingly given the ubiquity and fulsome display of plant photosynthesis. On the other hand, evidence for the existence of bacterial photosynthesis only emerged in the early 1900s.^{1,2} While the structural elucidation of bacteriochlorophyll *a* quickly followed that of chlorophyll *a*,^{3–5} the vast majority of physical studies of photosynthetic tetrapyrrole pigments over the years have focused on chlorophylls rather than bacteriochlorophylls. The disparity is striking given that bacterial photosynthesis is generally simpler than plant photosynthesis. The greater simplicity of the bacterial photosynthetic machinery stems from reliance on a single reaction center and the requirement for relatively reduced electron donors (e.g., H_2S), in turn precluding oxygen

evolution, whereas plants employ two reaction centers in a Z-scheme, derive electrons from water, and evolve oxygen.⁶

The study of bacterial photosynthesis continues to be a fertile area of investigation, perhaps owing to the rich diversity of photosynthetic bacteria. Issues of great importance concern not only the fundamental physical properties of individual bacteriochlorophylls but also the properties that emerge upon assembly of multiple bacteriochlorophylls into reaction center and antenna complexes. Of particular interest in these multichromophoric systems are the extent of excited-state delocalization and the role of possible electronic and/or vibrational coherence in mediating electron transfer and energy flow.^{7–14} Understanding interchromophore interactions is also fundamental to the design of covalently linked arrays of synthetic bacteriochlorins for use in solar-energy conversion. In

Received: May 1, 2014

Revised: June 6, 2014

Published: June 26, 2014



such arrays, a key issue concerns the electron density in the interacting molecular orbitals of the constituent chromophores.^{15–17}

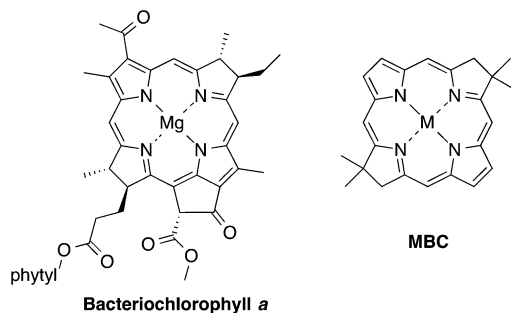
One approach to probing the spectroscopic and photo-physical properties of chromophores relies on isotopic substitution (e.g., ^2H , ^{13}C , ^{15}N). The bacteriochlorophylls of photosynthetic bacteria are tetrahydroporphyrins, whereas the chlorins of green plants are dihydroporphyrins. Bacteriochlorophylls have been reported to be somewhat unstable on routine handling;^{18,19} hence, studies concerning bacteriochlorophyll properties have often relied on synthetic bacteriochlorin surrogates. Indeed, *meso*-tetraphenylbacteriochlorin (derived by hydrogenation of *meso*-tetraphenylporphyrin) has been a widely studied synthetic bacteriochlorin. These studies encompass efforts wherein a variety of isotopologues have been employed, including the all- ^{15}N , all-*meso*- ^{13}C , all-phenyl- d_{20} , and β - d_8 species.^{20–28} While of great value, this palette of isotopically labeled species is still rather limited considering the number of chemically distinct positions in the bacteriochlorin macrocycle.

Recently, we exploited a *de novo* synthesis of bacteriochlorins to gain access to a much broader palette of bacteriochlorin isotopologues.²⁶ The *de novo* synthesis affords a bacteriochlorin chromophore with a geminal dimethyl group in each reduced, pyrrole ring, and no other substituents. Thus, the synthetic macrocycles lack the nearly full complement of peripheral substituents characteristic of the natural bacteriochlorophylls as shown in Chart 1. Each bacteriochlorin

of interest here contains a pair of ^{13}C or ^{15}N isotopes located symmetrically about the C_2 axis of the macrocycle (assuming a planar macrocycle with C_{2h} symmetry) as shown in Chart 2. The set of 24 macrocycles includes eight free base bacteriochlorins, of which six isotopomers contain a pair of ^{13}C isotopes and two isotopomers contain a pair of ^{15}N isotopes, and the copper and zinc chelates thereof.

In this paper, we report the spectroscopic characterization of 16 isotopically substituted bacteriochlorins (eight copper chelates and eight zinc chelates). The copper chelates were examined by resonance Raman (RR) and Fourier-transform infrared (FT-IR) spectroscopy; the zinc chelates, upon one-electron oxidation to the π -cation radical, were examined by electron paramagnetic resonance (EPR) spectroscopy. The spectroscopic studies are accompanied by density functional theory (DFT) calculations that are used to assign the vibrational spectra of the copper chelates and predict the spin-density distributions in the π -cation radicals of the zinc chelates. The studies yield certain unexpected results: (1) An exceptional sparsity of vibronically active normal modes of the core neutral bacteriochlorin macrocycle. (2) Spin-density distributions in the π -cation radical that are substantially different from those previously reported for these species and assumed to be correct for nearly four decades. These findings have implications for how the structural features that characterize natural bacteriochlorophylls might influence energy- and electron-transfer processes in photosynthesis and alter the thinking on the design of synthetic, bacteriochlorin-based arrays for solar-energy conversion.

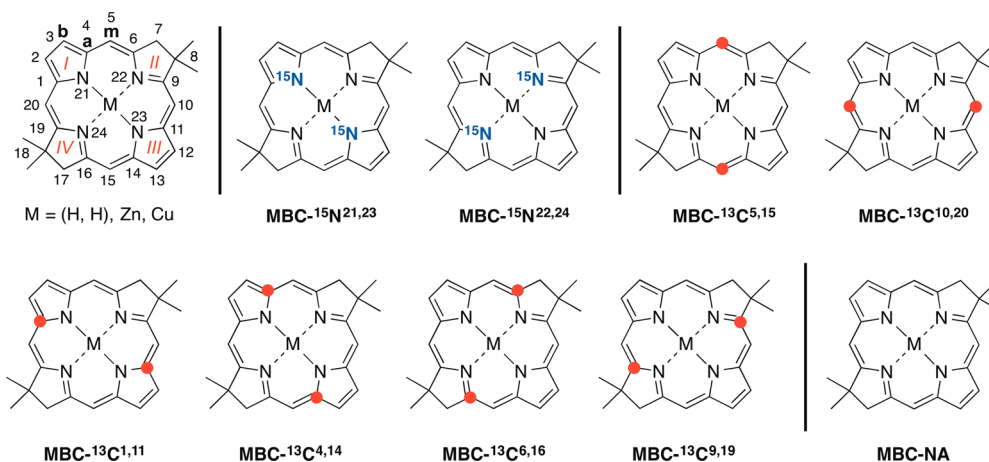
Chart 1. Structures of Native and Synthetic Bacteriochlorins



II. EXPERIMENTAL SECTION

A. Nomenclature. The natural abundance bacteriochlorins are indicated with the suffix “NA” (e.g., $\text{H}_2\text{BC-NA}$), whereas the bacteriochlorins with specific isotopic substitution are indicated with a suffix, indicating the position and nature of the isotope (e.g., $\text{H}_2\text{BC-}^{13}\text{C}^{4,14}$). Compound names without suffix labels for a particular isotopic species are used to refer to properties that are general to all the natural abundance and isotopologue species. The metalation state of the macrocycle is indicated with a prefix as shown in Chart 2.

Chart 2. Macrocycle Numbering and Labeling Scheme for MBC (Upper Left) and the Location of the Isotopic Substitutions (Red ● = ^{13}C)^a



^aNote that there are two resonance structures for the bacteriochlorin.

B. Synthesis. $\text{H}_2\text{BC-NA}$, CuBC-NA , ZnBC-NA , and the free base and metal chelates of the various isotopologues were prepared as previously described.²⁶ The NMR spectral properties of the free base and zinc chelates also have been reported.²⁷ These studies have shown that the synthesized free bases of all the isotopologues are >98% doubly labeled, with the exceptions of $\text{H}_2\text{BC-}^{13}\text{C}^{4,14}$ and $\text{H}_2\text{BC-}^{15}\text{N}^{22,24}$. Each of these two isotopologues contains 74–75% doubly labeled and 23–24% singly labeled species. Consequently, the metalated complexes of these two isotopologues also contain these proportions of doubly and singly labeled species.

C. Absorption Spectroscopy. The absorption spectra of all the complexes were obtained at room temperature on samples in CH_2Cl_2 solutions contained in a 1 mm path length cell using a diode array spectrometer (HP8452).

D. RR Spectroscopy. The RR spectra of CuBC-NA and the isotopologues were obtained at room temperature on samples (~ 0.2 mM) in CH_2Cl_2 solutions contained in 5 mm diameter NMR tubes that had been cut to a length of ~ 4 cm. The NMR tube was spun to mitigate photodamage. The RR spectra obtained with UV–visible excitation were acquired with a triple spectrograph (Spex 1877) equipped with a holographically etched 2400 groove/mm grating (UV excitation) or 1800 groove/mm grating (visible excitation) in the third stage. A UV-enhanced charge-coupled device (CCD) was used as the detector (Princeton Instruments LN/CCD equipped with an EEV1152-UV chip). The RR spectra obtained with near-infrared excitation were acquired with a red-optimized triple spectrograph (Spex 1877) equipped with a holographically etched 1200 groove/mm grating in the third stage. A back-illuminated (CCD) was used as the detector (Princeton Instruments LN/CCD equipped with a Tektronix chip). The excitation wavelengths of 371, 502, and 730 nm were provided by the discrete outputs of a diode laser (Crystalaser DL-375-026-S), an argon ion laser (Coherent Innova 400–15UV), or a Ti:sapphire laser (Coherent 890), pumped by a diode-pumped solid-state laser (Coherent Verdi-V6), respectively. The laser powers were typically in the 8–9 mW range; the beam diameter was ~ 0.5 mm. The scattered light was collected in a 90° configuration by using a 50 mm camera lens ($f/1.4$ for UV–visible and $f/1.2$ for near-infrared excitation). The spectra were acquired with 0.5 to 2 h of signal averaging (10×180 s to 40×180 s scans). The spectral resolution was ~ 2 cm^{-1} at a Raman shift of 200 cm^{-1} . The spectral data were calibrated using the known frequencies of indene²⁸ and fenchone.²⁹

E. FT-IR Spectroscopy. The FT-IR spectra of CuBC-NA and the isotopologues were obtained at room temperature on samples (1–2% by wt) in KBr pellets using a spectrometer (Bruker Equinox 55) equipped with a DTGS detector. The spectra were acquired with 1400 scans at a spectral resolution of 4 cm^{-1} .

F. Electrochemistry. All electrochemical measurements on ZnBC-NA and the isotopologues as well as sample preparations for EPR studies of the monocations of the complexes were performed at room temperature in an inert atmosphere glovebox. Voltammetry and bulk electrolysis experiments were performed using a three-compartment glass cell with compartments separated by ultrafine glass frits. The working electrode for voltammetry was a 0.5 mm diameter Pt wire and the working electrode for bulk electrolysis was a 1 cm^2 Pt mesh. The auxiliary electrode was a 1 cm^2 Pt mesh. The reference electrode consisted of two stages. The first stage is composed of a 0.5 mm diameter Ag wire in a Ag^+ solution (10 mM AgPF_6 ,

100 mM Bu_4NPF_6 (TBAH) in butyronitrile). The second stage contains a solution of 100 mM TBAH in butyronitrile as an isolation bridge between the first stage and the sample cell. The stages of the reference cell and the bridge/sample cell interfaces are separated by porous Vycor frits.

G. EPR Spectroscopy and Spectral Simulations. EPR spectra of $[\text{ZnBC-NA}]^+$ and the monocations of the isotopologues were obtained at room temperature on samples (0.2–0.3 mM) in TBAH (100 mM)/ CH_2Cl_2 solutions using an X-band spectrometer (Bruker EMX) equipped with a NMR gaussmeter and microwave frequency counter. The microwave power and magnetic field modulation amplitude were typically 6.33 mW and 0.3 G, respectively. The EPR spectra were simulated to obtain the hyperfine coupling constants using the WinSim 2002 program.³⁰

H. Computational Methods. DFT calculations were performed to obtain optimized geometries, vibrational frequencies, and hyperfine coupling constants and spin densities using Gaussian '09, revision D.01.³¹ The geometries for CuBC , ZnBC , and $[\text{ZnBC}]^+$ were obtained at the B3LYP/6-31+G(d,p) level using very tight optimization; the grids for the neutral and cation radical species were ultrafine and superfine, respectively.

The vibrational frequencies and normal modes for CuBC-NA were calculated at the B3LYP/6-31+G(d,p) level using an ultrafine grid. The vibrational frequencies for the isotopologues were obtained using the GaussView program.³² The vibrational frequencies reported are scaled by the correction factor of 0.97. The potential energy distributions (PEDs) were calculated using the VEDA4 program.³³ Input to the VEDA4 program was obtained from the frequency calculation formatted checkpoint file (molecular structure and force constants) and internal coordinates as defined in the Z-matrix for the geometry optimization calculation.

The spin densities and hyperfine coupling constants for $[\text{ZnBC}]^+$ were obtained from calculations performed at the TPSSH/aug-cc-pVTZ-J level³⁴ on geometries optimized as described above. The aug-cc-pVTZ-J basis set was obtained from the online Basis Set Exchange.^{35,36} The SCF convergence was set to the key word “sleazy” to reduce tolerances owing to limited convergence.

III. RESULTS

A. Absorption Spectra. The absorption spectrum of CuBC-NA is shown in Figure 1. The spectrum is similar to that previously reported for $\text{H}_2\text{BC-NA}$,³⁷ ZnBC-NA ,³⁸ and bacteriochlorins in general.^{39,40} The spectrum of CuBC-NA exhibits four prominent bands: $Q_y(0,0)$, 730 nm; $Q_x(0,0)$, 505 nm; $B_x(0,0)$, 375 nm; and $B_y(0,0)$, 331 nm. The two transitions that are polarized along the y axis, which bisects the pyrrole (unsaturated) rings, are comprised of linear combinations of promotions from the highest occupied molecular orbital (HOMO) to the lowest unoccupied molecular orbital (LUMO) and the HOMO–1 to LUMO+1. The two transitions that are polarized along the x axis, which bisects the pyrroline (reduced) rings, are comprised of linear combinations of promotions from the HOMO to LUMO+1 and the HOMO–1 to LUMO. Vibronic satellites are observed on the high-energy sides of both the $Q_y(0,0)$ and $Q_x(0,0)$ bands of CuBC-NA (and the isotopologues), most prominently on the former band, appearing at 694 and 656 nm. Similar vibronic features are observed for $\text{H}_2\text{BC-NA}$ ³⁷ and ZnBC-NA (Figure S1 of the Supporting Information).³⁸ A noteworthy aspect of the vibronic

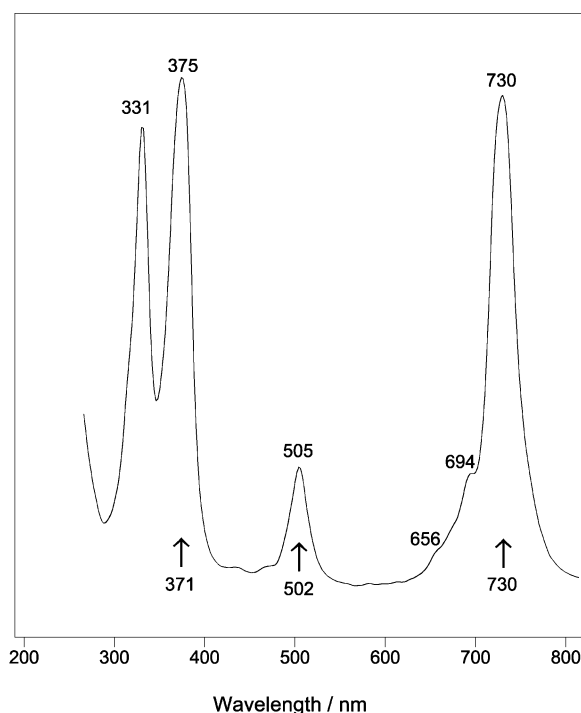


Figure 1. Absorption spectrum of **CuBC-NA** in CH_2Cl_2 solution. The arrows indicate the RR excitation lines.

features of all the molecules is that the strongest feature (~ 694 nm for **CuBC-NA**) lies ~ 700 – 730 cm^{-1} above the fundamental absorption (730 nm). This energy difference is smaller than that typically observed for tetrapyrroles, for which the vibronic envelope typically exhibits maximum intensity 1200–1500 cm^{-1} above the fundamental absorption.³⁹ It should also be noted that in the fluorescence spectrum of **ZnBC-NA** (**CuBC** is not fluorescent), a vibronic feature is observed in the 763–767 nm range, which is ~ 650 – 720 cm^{-1} lower in energy than the $Q_y(0,0)$ emission at 727 nm (Figure S1 of the Supporting Information).

B. Vibrational Spectra and Assignments for CuBC. The high-frequency regions of the RR spectra of **CuBC-NA** and the isotopologues acquired with Q_y , Q_x , and B_x excitation are shown in Figures 2, 3, and 4, respectively. The exact excitation wavelengths are indicated in the figures and marked by the arrows on the absorption spectrum shown in Figure 1. The low-frequency regions of the RR spectra of **CuBC-NA** acquired with Q_y , Q_x , and B_x -excitation are shown in Figure 5. The low-frequency RR spectra of the isotopologues were not examined in detail (vide infra). The high-frequency regions of the FT-IR spectra of **CuBC-NA** and the isotopologues are shown in Figure 6. The low-frequency FT-IR spectra were not examined for any of the complexes (vide infra).

The RR spectra of **CuBC-NA** and the isotopologues in the 900–1700 cm^{-1} region obtained with all excitation wavelengths are extremely sparse, exhibiting only 3–5 bands of any appreciable intensity and a comparable number of much weaker bands. Isotope shifts are apparent for most of the bands, the magnitude of which depends on the isotopomer. [Note that in the case of **CuBC- $^{13}\text{C}^{4,14}$** and **CuBC- $^{15}\text{N}^{22,24}$** , any contributions to spectra arising from the singly labeled species are not resolved.] The RR spectra in the 150–900 cm^{-1} region are similarly sparse, exhibiting only 3–5 bands of any appreciable intensity. The most striking feature of the low-

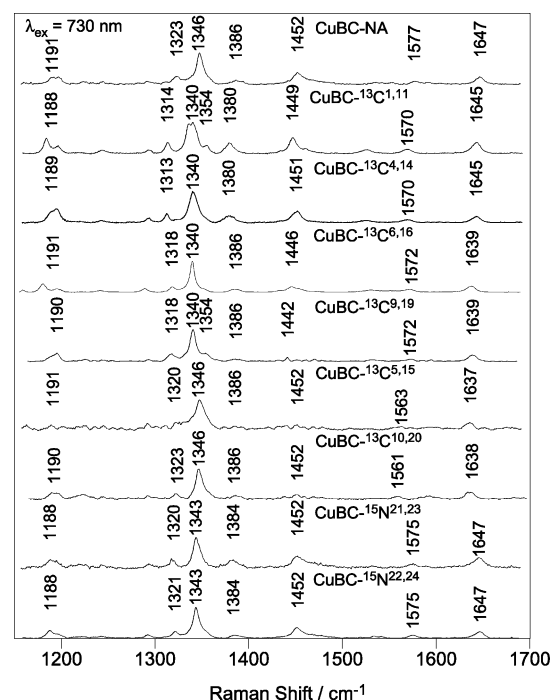


Figure 2. High-frequency regions of the Q_y -excitation ($\lambda_{\text{ex}} = 730$ nm) RR spectra of **CuBC-NA** and the isotopologues in CH_2Cl_2 solutions.

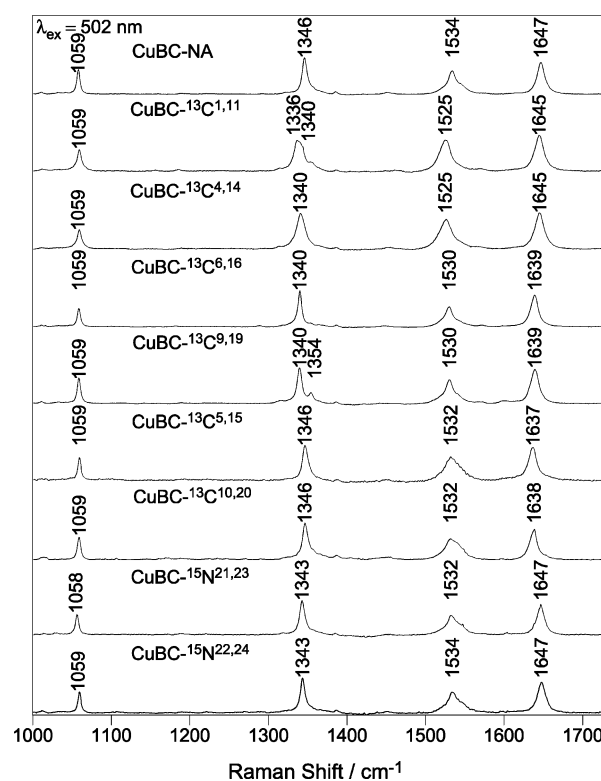


Figure 3. High-frequency regions of the Q_x -excitation ($\lambda_{\text{ex}} = 502$ nm) RR spectra of **CuBC-NA** and the isotopologues in CH_2Cl_2 solutions.

frequency RR spectra is observed with Q_y excitation, wherein an intense band at 727 cm^{-1} dominates the spectrum. The intensity of this band is 10-fold greater than any other band observed with Q_y excitation (Figure 5, top). A band is also observed in this spectral region with Q_x and B_x excitation (727 and 730 cm^{-1} , respectively); however, the intensity of the

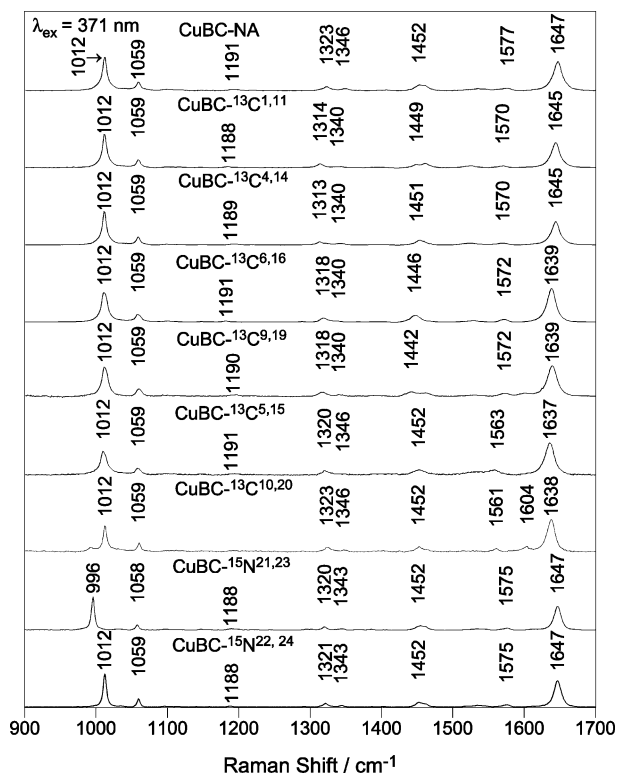


Figure 4. High-frequency regions of the B_x -excitation ($\lambda_{\text{ex}} = 371$ nm) RR spectra of **CuBC-NA** and the isotopologues in CH_2Cl_2 solutions.

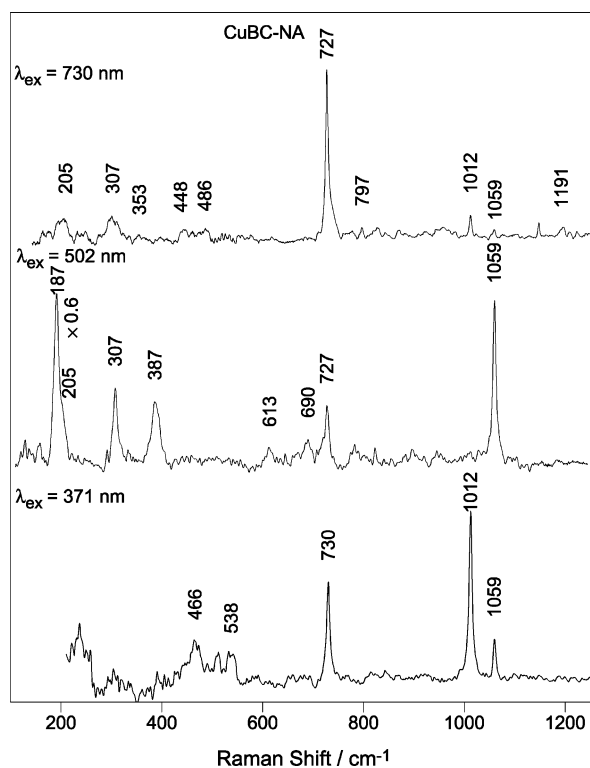


Figure 5. Low-frequency regions of the RR spectra of **CuBC-NA** in CH_2Cl_2 solution obtained with Q_y ($\lambda_{\text{ex}} = 730$ nm) (top), Q_x ($\lambda_{\text{ex}} = 502$ nm) (middle), and B_x ($\lambda_{\text{ex}} = 371$ nm) (bottom) excitation.

bands with these excitation wavelengths is more comparable to that of the other bands in the spectra. The dearth of resonantly enhanced Raman bands in the spectra of **CuBC-NA** and the

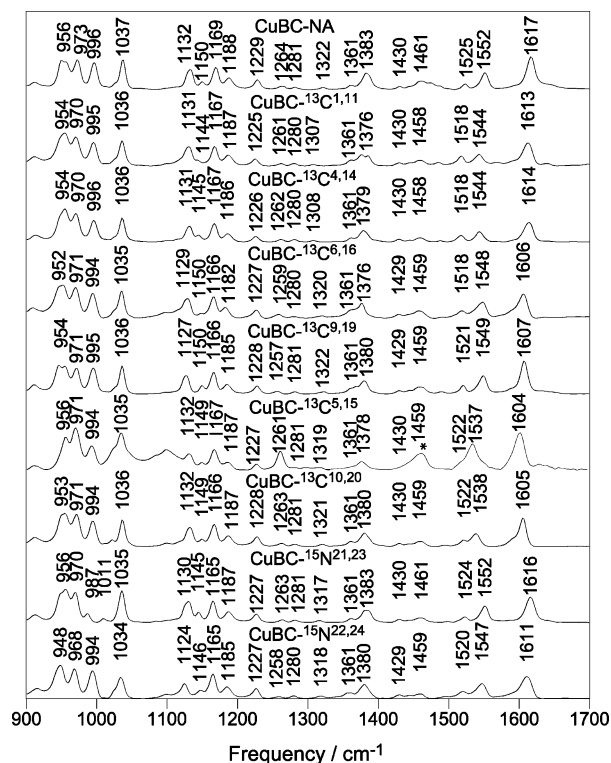


Figure 6. High-frequency regions of the FT-IR spectra of **CuBC-NA** and the isotopologues in KBr pellets. In the spectrum of **CuBC-13C5,15**, the band near 1462 cm^{-1} (asterisk) is due to a minor impurity.

isotopologues, and in particular, in the low-frequency regions, makes a detailed assignment of the spectra more difficult. For this reason, the low-frequency RR spectra of the isotopologues were not examined in detail.

The FT-IR spectra of **CuBC-NA** and the isotopologues are richer than the RR spectra. As is the case for the RR spectra, a number of the bands in the FT-IR spectra exhibit isotope shifts. [The FT-IR spectra of **CuBC-13C4,14** and **CuBC-15N22,24** also do not exhibit distinguishable features due to the singly labeled species.] Much of the increase in spectral complexity in the FT-IR versus RR spectra arises from the presence of bands in the former spectra that are principally due to bending modes involving the hydrogen atoms in the $\text{C}^{8,18}$ -methyl groups and the hydrogen atoms bonded directly to the macrocycle, rather than additional vibrations associated with the bacteriochlorin skeleton (vide infra). The carbon–hydrogen bending modes also contribute to the low-frequency regions of the FT-IR spectra. The increased spectral complexity in the low-frequency FT-IR spectra precludes accurate assignments; thus, the spectra in this region were not examined. The relatively sparse RR spectra also preclude further refinement of empirical vibrational force fields for **MBC** complexes, beyond those already reported.^{22,23}

Closer examination of the RR versus FT-IR spectra of **CuBC-NA** and the isotopologues reveals that the spectra are mutually exclusive in terms of the bands observed. This observation suggests that the molecule has an inversion center. This prediction is supported by calculations, which indicate that the minimum-energy structure of **CuBC** exhibits C_i symmetry. This symmetry arises because pyrroline rings II and IV are slightly twisted (otherwise the macrocycle core is nearly planar), with the $\text{C}^6\text{--C}^7\text{--C}^8\text{--C}^9$ torsional angle of pyrroline

Table 1. Vibrational Frequencies, Isotope Shifts, and Potential Energy Distributions (PEDs) for CuBC

| CuBC-NA | | frequency (cm ⁻¹) | | | | | | | | | | | | PED ^a | | | | | |
|----------------|------|-------------------------------|------|------------------------------|------|------------------------------|------|------------------------------|------|------------------------------|------|-------------------------------|------|------------------|------|------------------------------|---|---|---|
| | | $\Delta^{13}\text{C}^{1,11}$ | | $\Delta^{13}\text{C}^{4,14}$ | | $\Delta^{13}\text{C}^{6,16}$ | | $\Delta^{13}\text{C}^{9,19}$ | | $\Delta^{13}\text{C}^{5,15}$ | | $\Delta^{13}\text{C}^{10,20}$ | | | | $\Delta^{15}\text{N}^{2,24}$ | | | |
| | obsd | calcd | obsd | calcd | obsd | calcd | obsd | calcd | obsd | calcd | obsd | calcd | obsd | calcd | obsd | calcd | | | |
| A _g | | | | | | | | | | | | | | | | | | | |
| 1 | 1647 | 1645 | -2 | -2 | -4 | -8 | -10 | -8 | -9 | -10 | -13 | -9 | -11 | 0 | 0 | 0 | 41% $\nu\text{C}_3\text{C}_m(\text{II,IV})$, 21% $\nu\text{C}_3\text{C}_m(\text{I,III})$ | | |
| 2 | 1577 | 1572 | -7 | -6 | -7 | -6 | -5 | -4 | -5 | -14 | -17 | -16 | -18 | -2 | 0 | -2 | 0 | 31% $\nu\text{C}_3\text{C}_m(\text{I,III})$, 25% $\nu\text{C}_3\text{C}_m(\text{II,IV})$, 13% $\nu\text{C}_3\text{C}_b(\text{I,II,III,IV})$ | |
| 3 | 1534 | 1536 | -9 | -11 | -9 | -11 | -4 | -5 | -4 | -2 | -2 | -2 | -2 | 0 | 0 | 0 | 0 | 18% $\delta\text{C}_3\text{C}_3\text{C}_b(\text{I,III})$, 17% $\nu\text{C}_3\text{C}_m(\text{I,III})$, 10% $\delta\text{C}_3\text{C}_3\text{C}_b(\text{I,III})$, 10% $\nu\text{C}_3\text{C}_b(\text{I,III})$ | |
| 4 | 1452 | 1455 | -3 | -5 | -1 | 0 | -6 | -5 | -10 | -5 | 0 | -1 | 0 | -2 | 0 | 0 | -1 | 30% $\nu\text{C}_3\text{C}_b(\text{I,III})$, 10% $\nu\text{C}_3\text{C}_m$, 10% $\delta\text{C}_3\text{C}_3\text{C}_b(\text{II,IV})$ | |
| 5 | 1386 | 1383 | -6 | -1 | -6 | -3 | 0 | -2 | 0 | -1 | 0 | 0 | 0 | -2 | -1 | -2 | -1 | 84% $\delta\text{C}_3\text{C}_m\text{H}$ | |
| 6 | 1346 | 1333 | -6 | -10 | -6 | -9 | -6 | -6 | -6 | 0 | 0 | 0 | -1 | -3 | -3 | -4 | -4 | 20% $\nu\text{C}_3\text{C}_3(\text{I,III})$, 20% $\delta\text{C}_3\text{C}_3\text{N}(\text{I,II,III,IV})$, 11% $\nu\text{C}_3\text{C}_3(\text{II,IV})$, 17% $\nu\text{C}_3\text{N}(\text{I,II,III,IV})$ | |
| 7 | 1323 | 1324 | -9 | -13 | -10 | -14 | -5 | -2 | -5 | -3 | -1 | 0 | 0 | -3 | -5 | -2 | -1 | 17% $\delta\text{C}_3\text{C}_3\text{C}_b(\text{I,III})$, 13% $\{\delta\text{C}_3\text{C}_b\text{H}(\text{I,III})$, $\delta\text{C}_3\text{C}_b\text{H}(\text{I,III})\}$, 12% $\nu\text{C}_3\text{N}(\text{I,III})$, 10% $\delta\text{C}_3\text{C}_3\text{H}(\text{I,II})$, 10% $\delta\text{C}_3\text{C}_3\text{N}(\text{I,III})$ | |
| 8 | 1191 | 1186 | -3 | -1 | -2 | -1 | 0 | -1 | -1 | -2 | 0 | -1 | -1 | 0 | -3 | -1 | -3 | -2 | 16% $\nu\text{C}_3\text{C}_b(\text{I,II,III,IV})$, 10% $\nu\text{C}_3\text{N}(\text{I,II,III,IV})$, 10% $\delta\text{C}_3\text{C}_3\text{H}(\text{I,III})$ |
| 9 | 1059 | 1053 | 0 | 0 | 0 | 0 | 0 | 0 | 0 | 0 | 0 | 0 | 0 | 0 | -1 | 0 | 0 | 68% $\{\delta\text{C}_3\text{C}_3\text{H}(\text{I,III})$, $\delta\text{C}_3\text{C}_b\text{H}(\text{I,III})\}$ | |
| 10 | 1012 | 997 | 0 | 0 | 0 | 0 | 0 | 0 | 0 | 0 | -1 | 0 | -1 | -16 | -16 | 0 | 0 | 32% $\nu\text{C}_3\text{C}_b(\text{I,III})$, 29% $\delta\text{C}_3\text{C}_3\text{N}(\text{I,III})$, 10% $\nu\text{C}_3\text{N}(\text{I,III})$ | |
| A _u | | | | | | | | | | | | | | | | | | | |
| 11 | 1617 | 1604 | -4 | -2 | -3 | -3 | -11 | -10 | -10 | -9 | -13 | -12 | -11 | -1 | 0 | -6 | 0 | 47% $\nu\text{C}_3\text{C}_m(\text{II,IV})$, 15% $\nu\text{C}_3\text{C}_m(\text{I,III})$ | |
| 12 | 1552 | 1550 | -8 | -7 | -8 | -7 | -4 | -3 | -3 | -2 | -15 | -14 | -14 | 0 | 0 | -5 | -2 | 18% $\nu\text{C}_3\text{C}_m(\text{II,IV})$, 13% $\nu\text{C}_3\text{C}_b(\text{I,III})$, 12% $\delta\text{C}_3\text{C}_3\text{C}_b(\text{I,IV})$ | |
| 13 | 1525 | 1528 | -7 | -5 | -7 | -6 | -7 | -4 | -4 | -3 | -3 | -2 | -3 | -1 | 0 | -5 | -1 | 19% $\delta\text{C}_3\text{C}_3\text{C}_b(\text{I,III})$, 17% $\nu\text{C}_3\text{C}_b(\text{I,III})$, 16% $\{\delta\text{C}_3\text{C}_b\text{H}(\text{I,III})$, $\delta\text{C}_3\text{C}_b\text{H}(\text{I,III})\}$, 12% $\nu\text{C}_3\text{C}_m(\text{II,IV})$ | |
| 14 | 1461 | 1463 | -3 | 0 | -3 | 0 | -2 | 0 | -2 | 0 | -2 | 0 | 0 | 0 | 0 | -2 | 0 | 75% $\{\tau\text{C}_3\text{C}_3\text{C}_3\text{C}_m\text{H}$, $\tau\text{C}_3\text{C}_3\text{C}_3\text{C}_m\text{H}\}$, 22% $\delta\text{C}_3\text{C}_m\text{H}$ | |
| 15 | 1430 | 1438 | 0 | 0 | 0 | 0 | -1 | 0 | -1 | 0 | 0 | 0 | 0 | 0 | 0 | -1 | 0 | 60% $\tau\text{C}_3\text{C}_3\text{C}_3\text{C}_b\text{H}(\text{II,IV})$, 18% $\delta\text{C}_3\text{C}_3\text{H}(\text{II,IV})$, 18% $\{\tau\text{C}_3\text{C}_3\text{C}_3\text{C}_m\text{H}$, $\tau\text{C}_3\text{C}_3\text{C}_3\text{C}_m\text{H}\}$ | |
| 16 | 1383 | 1380 | -7 | -6 | -4 | -5 | -7 | -4 | -3 | -3 | -5 | -2 | -3 | 0 | -2 | -3 | 0 | 37% $\nu\text{C}_3\text{C}_b(\text{I,III})$, 15% $\{\delta\text{C}_3\text{C}_3\text{H}(\text{I,III})$, $\delta\text{C}_3\text{C}_b\text{H}(\text{I,III})\}$, 12% $\delta\text{C}_3\text{C}_m\text{H}(\text{I,II})$ | |
| 17 | 1361 | 1361 | 0 | 0 | 0 | 0 | 0 | -1 | 0 | 0 | 0 | 0 | 0 | 0 | 0 | 0 | 0 | 96% $\delta\text{C}_3\text{C}_m\text{H}$ | |
| 18 | 1322 | 1313 | -15 | -13 | -14 | -14 | -2 | 0 | -1 | -3 | -1 | -1 | -1 | -5 | -5 | -4 | 0 | 16% $\{\delta\text{C}_3\text{C}_b\text{H}(\text{I,III})$, $\delta\text{C}_3\text{C}_b\text{H}(\text{I,III})\}$, 15% $\nu\text{C}_3\text{N}(\text{I,III})$, 13% $\nu\text{C}_3\text{C}_b(\text{I,III})$, 12% $\nu\text{C}_3\text{C}_m(\text{I,III})$, 11% $\delta\text{C}_3\text{C}_3\text{C}_b(\text{I,III})$, 11% $\delta\text{C}_3\text{C}_3\text{N}(\text{I,III})$ | |
| 19 | 1281 | 1272 | -1 | -1 | -1 | -1 | -1 | -1 | 0 | 0 | -1 | 0 | 0 | 0 | 0 | -1 | -1 | 27% $\delta\text{C}_3\text{C}_b\text{H}(\text{II,IV})$ | |
| 20 | 1264 | 1246 | -3 | -1 | -2 | -3 | -5 | -7 | -7 | -7 | -3 | -1 | -1 | -1 | 0 | -6 | -5 | 22% $\nu\text{C}_3\text{C}_b(\text{II,IV})$, 20% $\{\delta\text{C}_3\text{C}_b\text{H}(\text{I,III})$, $\delta\text{C}_3\text{C}_b\text{H}(\text{I,III})\}$ | |
| 21 | 1229 | 1219 | -4 | -4 | -3 | -3 | -2 | -2 | -1 | -2 | 0 | -1 | 0 | -2 | -2 | -2 | -1 | 12% $\delta\text{C}_3\text{C}_b\text{H}(\text{II,IV})$, 10% $\delta\text{C}_3\text{C}_m\text{H}$, 10% $\nu\text{C}_3\text{C}_m$ | |
| 22 | 1188 | 1183 | -1 | 0 | -2 | -1 | -6 | -5 | -3 | -4 | -1 | 0 | -1 | 0 | -1 | 0 | -3 | -2 | 12% $\nu\text{C}_3\text{C}_b(\text{II,IV})$, 11% $\nu\text{C}_3\text{C}_b(\text{II,IV})$, 10% $\nu\text{C}_3\text{N}(\text{II,IV})$ |
| 23 | 1169 | 1167 | -2 | -1 | -2 | -1 | -3 | -2 | -3 | -3 | -2 | -2 | -3 | -4 | -3 | -4 | -2 | 22% $\nu\text{C}_3\text{C}_m(\text{II,IV})$, 15% $\delta\text{C}_3\text{C}_m\text{H}(\text{I,II})$, 15% $\{\delta\text{C}_3\text{C}_b\text{H}(\text{I,III})$, $\delta\text{C}_3\text{C}_b\text{H}(\text{I,III})\}$ | |
| 24 | 1150 | 1146 | -6 | -4 | -5 | -2 | 0 | -3 | 0 | 0 | -1 | 0 | -1 | -5 | -2 | -4 | -3 | 22% $\{\delta\text{C}_3\text{C}_b\text{H}(\text{I,III})$, $\delta\text{C}_3\text{C}_b\text{H}(\text{I,III})\}$, 21% $\nu\text{C}_3\text{N}(\text{I,II,III,IV})$, 15% $\nu\text{C}_3\text{C}_b(\text{I,III})$ | |
| 25 | 1132 | 1139 | -1 | -2 | -1 | -4 | -3 | -1 | -5 | -5 | 0 | 0 | 0 | -2 | -4 | -8 | -9 | 19% $\delta\text{C}_3\text{C}_3\text{N}(\text{I,II,III,IV})$, 15% $\delta\text{C}_3\text{C}_3\text{H}(\text{I,III})$, 10% $\delta\text{C}_3\text{C}_m\text{H}$ | |
| 26 | 1037 | 1036 | -1 | -1 | -1 | 0 | -2 | -1 | -1 | -1 | -2 | -1 | -1 | 0 | -2 | 0 | -3 | 0 | 66% $\{\delta\text{C}_3\text{C}_b\text{H}(\text{I,III})$, $\delta\text{C}_3\text{C}_b\text{H}(\text{I,III})\}$, 12% $\nu\text{C}_3\text{C}_b(\text{I,III})$ |

^aMode descriptors: ν = stretch; δ = bend; τ = torsion. C_a , C_b , C_m , and I–IV refer to the macrocycle positions shown in Chart 2.

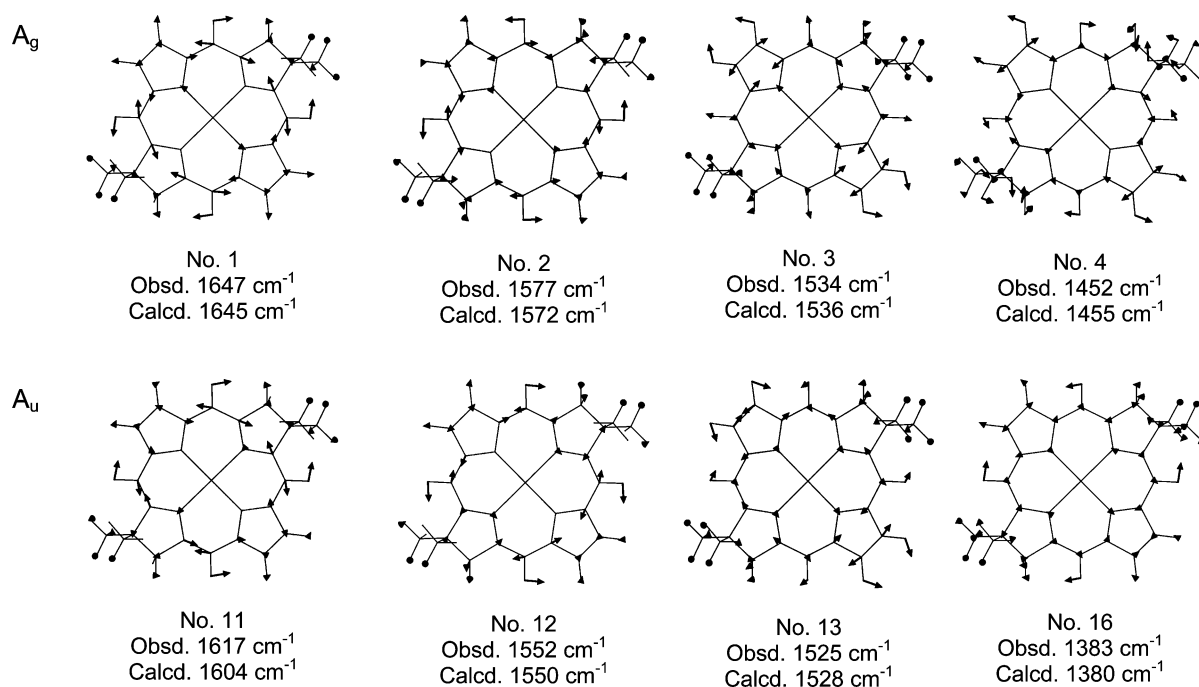


Figure 7. Vibrational eigenvectors (mass-weighted Cartesian coordinates) of selected A_g (top row) and A_u (bottom row) modes of CuBC that contain substantial $\nu C_a C_m$ or $\nu C_b C_b(I,III)$ character (see Table 1).

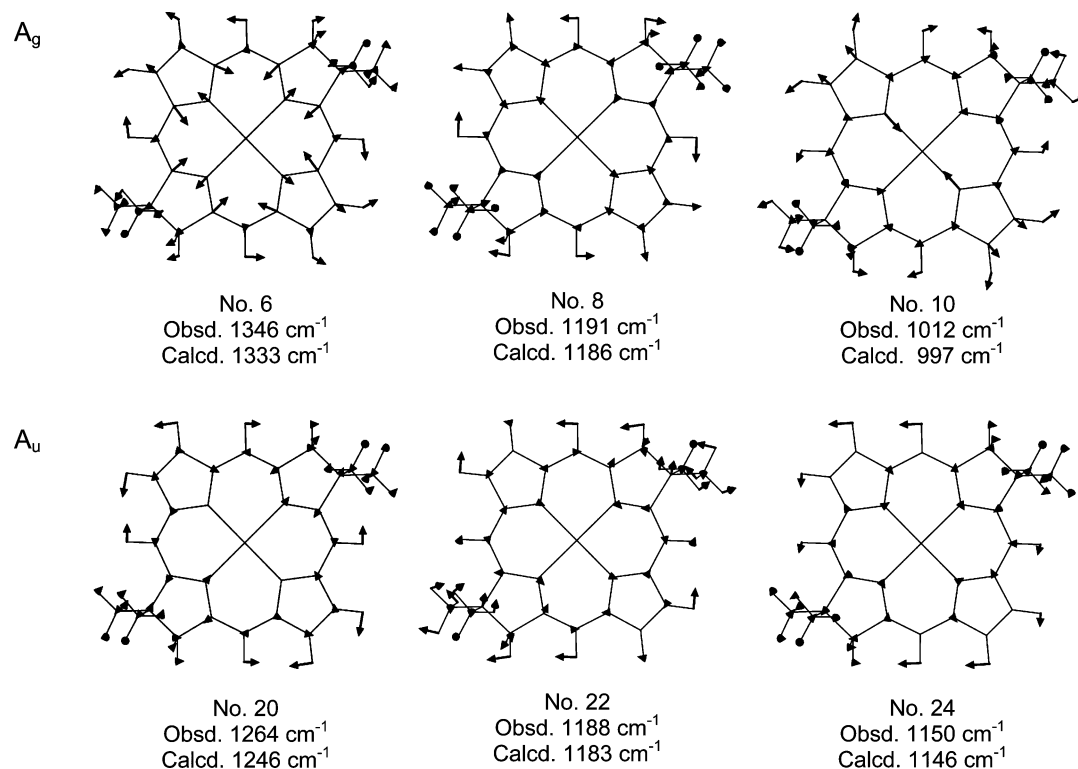


Figure 8. Vibrational eigenvectors (mass-weighted Cartesian coordinates) of selected A_g (top row) and A_u (bottom row) modes of CuBC that contain substantial $\nu C_a C_b$ or $\nu C_a N$ character (see Table 1).

ring II and $C^{16}-C^{17}-C^{18}-C^{19}$ torsional angle of pyrroline ring IV being equal ($\sim 15^\circ$) and opposite in sign. This distortion renders the C^7 hydrogen atom and C^8 methyl group that are above the (pseudo) plane of ring II equivalent to the C^8 hydrogen atom and C^{18} methyl group that are below the (pseudo) plane of ring IV (and vice versa). The C_i symmetry of the core macrocycle is further maintained at the level of the

torsional angles of the methyl groups. The calculated structure of CuBC is shown in Figure S2 of the Supporting Information; the structural parameters (bond lengths, bond angles, and torsional angles) are listed in Tables S1–S3 of the Supporting Information.

The observed and calculated vibrational frequencies, isotope shifts, and PEDs for CuBC are listed in Table 1. The table is

symmetry factored into A_g and A_u blocks appropriate for C_i symmetry, consistent with the calculated structure of CuBC and the mutual exclusion of the bands observed in the RR versus FT-IR spectra. Only those calculated bands that are assigned to observed bands are reported. The vibrational assignments listed in the table were made via systematic examination of the isotope shifts of a given band and choosing the calculated mode, wherein the frequency and isotope shifts are most consistent with those observed. The observed A_g vibrations are primarily bond stretches of the macrocycle; the A_u vibrations include bond stretches as well as carbon–hydrogen bending modes.

The vibrational eigenvectors for selected modes that are predominantly stretching vibrations of the methine bridges ($\nu_{C_aC_m}$) or C_bC_b bonds of the pyrrole rings [$\nu_{C_bC_b}(\text{I,III})$] are shown in Figure 7. The vibrational eigenvectors for selected modes that are predominantly stretching vibrations of the C_aC_b and C_aN bonds ($\nu_{C_aC_b}$ and ν_{C_aN}) of the pyrrole and pyrroline rings are shown in Figure 8. The vibrational eigenvectors of all other modes listed in Table 1 are shown in Figure S3 of the Supporting Information. Most of these vibrations have A_u symmetry and exhibit substantial contributions from carbon–hydrogen bending motions.

Only vibrational frequencies above 1000 cm^{-1} are listed in Table 1, owing to the uncertainties in assigning the low-frequency spectra (vide supra). However, one lower-frequency mode that deserves additional comment is the band at 727 cm^{-1} , which dominates the Q_y -excitation RR spectrum of CuBC (Figure 2). A plausible assignment for this band is a vibration with a calculated frequency of 713 cm^{-1} , which is due to a symmetrical deformation of the five-atom $C_m(C_aNC_a)_{\text{pyrrole}}C_m$ portion of the ring core that resembles an accordion-like motion. This deformation visually appears to elongate/contract the inner core of the macrocycle along the x axis (see animation in Figure S4 of the Supporting Information). Regardless, the calculations indicate that the main contributor to the polarizability derivative of this vibration is α_{yy} . There is a similar symmetrical deformation involving the five-atom $C_m(C_aNC_a)_{\text{pyrroline}}C_m$ portion of the core that visually appears to elongate/contract the macrocycle along the y axis (see animation in Figure S5 of the Supporting Information). The calculations predict that the frequency of the $C_m(C_aNC_a)_{\text{pyrroline}}C_m$ deformation is 716 cm^{-1} , and that the main contributor to the polarizability derivative is α_{xx} . Plausibly, the band RR observed at 730 cm^{-1} with B_x excitation (Figure 5) is due to this latter vibration.

C. EPR Spectra, Hyperfine Coupling Constants, and Spin-Density Distributions for [ZnBC] $^+$. The EPR spectra of [ZnBC-NA] $^+$ and the cations of the isotopologues are shown in Figure 9 (left panels). The spectra shown for [ZnBC- $^{13}\text{C}^{4,14}$] $^+$ and [ZnBC- $^{15}\text{N}^{22,24}$] $^+$ have been corrected via subtraction of the simulated spectrum of the singly labeled species (vide infra). The spectra of all the isotopologues are extremely rich, exhibiting a large number (several dozen) of lines due to hyperfine interactions between the unpaired electron and the ^1H , $^{14}\text{N}/^{15}\text{N}$, and ^{13}C nuclei. The spectra of all of the isotopologues are different from one another and different from those of [ZnBC-NA] $^+$. Closer inspection of the spectra reveals the following: (1) The spectra of [ZnBC- $^{15}\text{N}^{21,23}$] $^+$ and [ZnBC- $^{15}\text{N}^{22,24}$] $^+$ differ from one another, indicating that the hyperfine coupling constants of the pyrrolic and pyrroline nitrogen atoms are different. (2) The spectra of all the ^{13}C isotopologues exhibit features indicative of

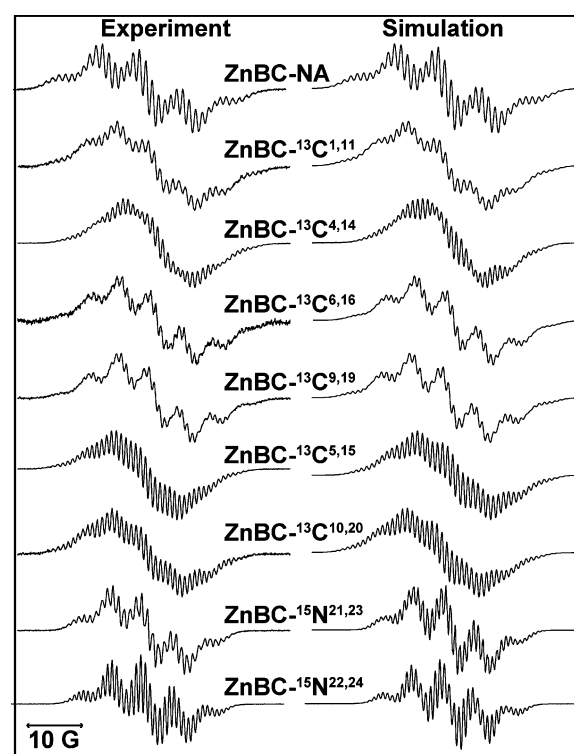


Figure 9. Observed and simulated EPR spectra of [ZnBC-NA] $^+$ and the monocations of the isotopologues in CH_2Cl_2 solutions. For [ZnBC- $^{13}\text{C}^{4,14}$] $^+$ and [ZnBC- $^{15}\text{N}^{22,24}$] $^+$ the contribution of the monoisotopically substituted species has been subtracted from the experimental spectra (see text).

hyperfine interactions, indicating spin density at the α -pyrrole, α -pyrroline, and *meso*-carbon atoms. (3) The spectral differences are least pronounced for isotopic substitutions at macrocycle sites that are structurally similar (e. g., the α -pyrroline carbon atoms, $\text{C}^{6,16}$ versus $\text{C}^{9,19}$) but rendered symmetry inequivalent by the presence of the $\text{C}^{7,17}$ hydrogen atoms versus $\text{C}^{8,18}$ methyl groups on the pyrroline rings.

The simulated EPR spectra of [ZnBC-NA] $^+$ and the cations of the isotopologues are shown in Figure 9 (right panels). The hyperfine coupling constants derived from the simulations are listed in Table 2. The simulations were conducted in a systematic fashion which began with examination of the natural abundance species, then proceeded to the two ^{15}N isotopomers, and finally to the six ^{13}C isotopomers.

In the simulation of the spectrum of [ZnBC-NA] $^+$, the initial set of hyperfine coupling constants for the four nitrogen, four pyrrolic hydrogen, and four pyrroline hydrogen atoms were set equal to those reported for the analogous atoms of [ZnTPBC-NA] $^+$. 21 For the latter complex, identical hyperfine coupling constants of 1.20 G were reported for the pyrrolic and pyrroline nitrogen atoms; hyperfine constants of 1.20 and 7.50 G were reported for the pyrrolic and pyrroline hydrogen atoms, respectively. The hyperfine coupling constants in this initial set were then allowed to float in attempts to simulate the EPR spectrum of [ZnBC-NA] $^+$. However, no satisfactory fit to the spectrum could be obtained. To obtain a reasonable fit, it was necessary to include hyperfine interactions from two additional sets of four hydrogen atoms, wherein the hyperfine coupling constants for the four atoms in a given set were the same. These hydrogen atoms could be those at the *meso* positions, methyl groups, or both; the exact identities cannot be

Table 2. Observed and Calculated Hyperfine Coupling Constants (a) and Calculated Spin Densities (ρ) for [ZnBC]⁺

| atom | a(G) | | ρ |
|--|-----------------------|------------|----------|
| | observed ^a | calculated | |
| ¹³ C ^{1,11} | 5.07 | 5.73 | 0.20 |
| ¹³ C ^{4,14} | 4.94 | 5.60 | 0.18 |
| ¹³ C ^{6,16} | 6.33 | 7.50 | 0.22 |
| ¹³ C ^{9,19} | 6.57 | 7.62 | 0.23 |
| ¹³ C ^{5,15} | (−)4.73 | −5.30 | −0.097 |
| ¹³ C ^{10,20} | (−)4.79 | −5.41 | −0.13 |
| ¹⁴ N ^{21,23} | (−)1.30 | −0.93 | −0.057 |
| ¹⁴ N ^{22,24} | (−)1.37 | −1.27 | −0.071 |
| ¹⁵ N ^{21,23} | 1.82 | 1.30 | −0.057 |
| ¹⁵ N ^{22,24} | 1.92 | 1.78 | −0.071 |
| ¹ H ^{2,12} | (−)1.19 | −1.38 | <i>b</i> |
| ¹ H ^{3,13} | (−)1.19 | −1.43 | <i>b</i> |
| ¹ H ^{5,15} | 1.10 | 1.04 | <i>b</i> |
| ¹ H ^{10,20} | 1.10 | 1.10 | <i>b</i> |
| ¹ H ^{7,17} | 6.75 | 9.26 | <i>b</i> |
| ¹ H ^{8,18} (Me) ^c | 0.80 | 0.74 | <i>b</i> |

^aObtained from simulations of the EPR spectra (see text). The signs are inferred from those of the calculated values; the opposite signs for ¹⁴N and ¹⁵N are due to the negative magnetogyric ratio of the latter nucleus. ^bValue ≤ 0.01 . ^cOnly one of the three hydrogens on each of the four equivalent methyl groups is included in the simulations (see text).

determined without examination of a set of deuteriated isotopologues. Regardless, all 12 of the methyl hydrogen atoms cannot be contributing significantly to the EPR spectrum because interactions with only eight additional hydrogen atoms provide a satisfactory fit. This final fit led to values of the hyperfine coupling constants of approximately 1.3, 1.2, and 6.8 G for the nitrogen, pyrrolic, and pyrrolic hydrogen atoms, respectively, and approximately 1.1 and 0.8 G for the two additional sets of hydrogen atoms.

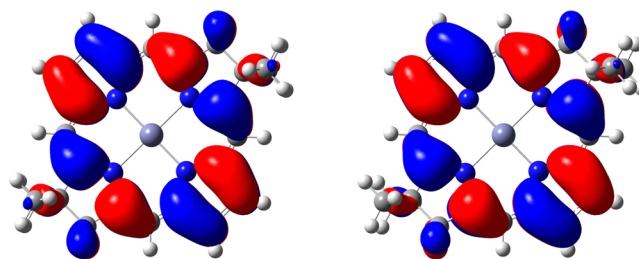
Simulations were then performed on the EPR spectra of [ZnBC-¹⁵N^{21,23}]⁺ and [ZnBC-¹⁵N^{22,24}]⁺. In the initial simulations, the values for the hyperfine coupling constants derived from simulations of the spectrum of [ZnBC-NA]⁺ were used, the only adjustment being scaling the coupling constant for the ¹⁵N atoms commensurate with the relative magnitude of the magnetogyric ratios of the two types of nitrogen nuclei [$\gamma(^{15}\text{N})/\gamma(^{14}\text{N}) \sim 1.40$; note that the magnetogyric ratio of ¹⁵N is negative⁴¹]. This afforded a reasonable fit to the spectra. However, the fits were improved by allowing minor adjustments in the values for the pyrrolic versus pyrrolic nitrogen atoms. In this fitting process, the EPR spectra of [ZnBC-NA]⁺, [ZnBC-¹⁵N^{21,23}]⁺, and [ZnBC-¹⁵N^{22,24}]⁺ were all examined to obtain the most self-consistent fit. The fitting process included accounting for the contribution of the singly labeled species to the EPR spectrum of [ZnBC-¹⁵N^{22,24}]⁺. The fitting process ultimately led to ¹⁴N hyperfine coupling constants of 1.30 and 1.37 G for the pyrrolic and pyrrolic nitrogen atoms, respectively. The adjustments to the hyperfine coupling constants of the two types of nitrogen atoms necessitated only very minor adjustments to the hyperfine coupling constants of the various hydrogen atoms, with final values of 1.10 and 6.75 G for the pyrrolic and pyrrolic hydrogen atoms, respectively, and 1.10 and 0.80 for the other two sets of

hydrogen atoms. The assignment in Table 2 of one of the latter two sets of hydrogen atoms to the four at the *meso*-carbon atoms and the other set to four on the methyl groups (one on each) will be discussed below.

Simulations were then performed on each of the six ¹³C isotopologues. In these simulations, the hyperfine coupling constants for the nitrogen and various hydrogen atoms were held constant at the values determined in the simulations of the spectra of [ZnBC-NA]⁺, [ZnBC-¹⁵N^{21,23}]⁺, and [ZnBC-¹⁵N^{22,24}]⁺. The simulations for [ZnBC-¹³C^{4,14}]⁺ accounted for the presence of singly labeled species. The simulations led to the ¹³C hyperfine coupling constants in the range of 4.9–5.2 G and 6.3–6.6 G for the α -pyrrole and α -pyrrolic carbon atoms, respectively, and 4.7–4.8 G for the *meso*-carbon atoms. The hyperfine coupling constants are slightly different for the symmetry inequivalent (by virtue of the C^{7,17} hydrogen atoms versus C^{8,18} methyl groups) pairs of α -carbon atoms in the pyrrolic rings [$a(^{13}\text{C}^{1,11})$, 5.07 G; $a(^{13}\text{C}^{4,14})$, 4.94 G] and the pyrrolic rings [e.g., $a(^{13}\text{C}^{6,16})$, 6.33 G; $a(^{13}\text{C}^{9,19})$, 6.57 G], as well as the two symmetry inequivalent pairs of carbon atoms at the *meso* positions [$a(^{13}\text{C}^{5,15})$, 4.73 G; $a(^{13}\text{C}^{10,20})$, 4.79 G].

To gain further insights into hyperfine interactions in [ZnBC]⁺ and the spin-density distributions that lead to the observed coupling constants, calculations were performed on the minimum-energy structure for [ZnBC]⁺. The calculated structural parameters (bond lengths, bond angles, torsional angles) for both cation and the parent neutral complex are listed in Tables S1–S3 of the Supporting Information. The calculated structural differences between [ZnBC]⁺ and ZnBC are relatively minor and primarily involve bond-length differences in the inner core of the macrocycle that are 0.02 Å or less. One noteworthy difference in the structure of [ZnBC]⁺ versus ZnBC is that the macrocycle of the former complex is planar, resulting in overall C_{2h} symmetry, whereas the pyrrolic rings of the latter complex are slightly distorted from planarity, resulting in C_i symmetry (as is also the case for CuBC). In the case of ZnBC, the C⁶–C⁷–C⁸–C⁹ torsional angle of ring II (and the C¹⁶–C¹⁷–C¹⁸–C¹⁹ torsional angle of ring IV) is slightly less ($\sim 10^\circ$) than that of CuBC ($\sim 15^\circ$). The C_{2h} symmetry of the core [ZnBC]⁺ macrocycle is further maintained at the level of the torsional angles of the methyl groups, rendering all four methyl groups equivalent.

The minor structural differences between [ZnBC]⁺ and ZnBC result in electron-density distributions in the singly occupied molecular orbital (SOMO) of the former complex that are very similar to those in the HOMO of the latter complex, as is shown in Figure 10. The SOMO of [ZnBC]⁺ exhibits substantial electron density on the α -pyrrole and α -pyrrolic carbon atoms, as expected for the a_{1u}-like SOMO of

**Figure 10.** Electron-density plots for the SOMO of [ZnBC]⁺ (left) and the HOMO of ZnBC (right).

bacteriochlorins in general (where the symmetry label refers to the D_{4h} symmetry of a parent metalloporphyrin molecule).^{21,39} However, the SOMO of $[\text{ZnBC}]^+$ (and the HOMO of ZnBC) also exhibit substantial electron density at the *meso*-carbon atoms, a prediction at odds with early calculations,²¹ but generally consistent with the substantial (4.7–4.8 G) *meso*- ^{13}C hyperfine coupling constants observed for the isotopologues.

The calculated hyperfine coupling constants and spin densities for all the atoms of $[\text{ZnBC}]^+$ are shown in Figure 11. The calculated hyperfine coupling constants and spin

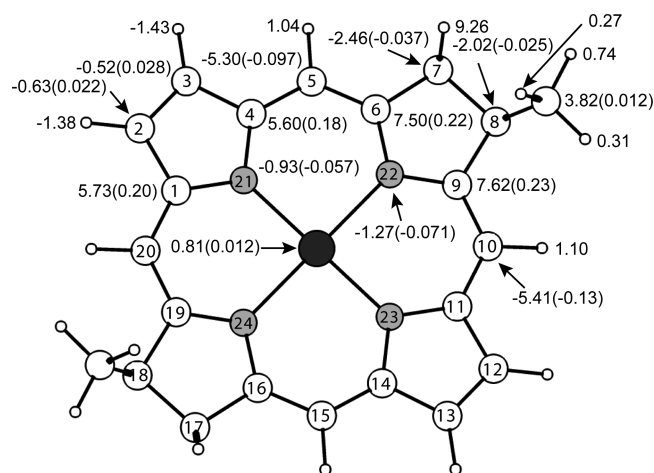


Figure 11. Structure of $[\text{ZnBC}]^+$ with calculated hyperfine coupling constants and spin densities (parentheses). The $\text{C}^{7,17}$ hydrogen atoms and $\text{C}^{8,18}$ methyl groups that are below the plane of the ring are omitted for clarity. The hyperfine coupling constants shown for the nitrogen atoms and zinc ion are for the ^{14}N and ^{67}Zn isotopes, respectively. The spin densities for all the hydrogen atoms are ≤ 0.01 and are omitted for clarity.

densities for those atoms wherein hyperfine coupling constants have been derived from the simulations of the EPR spectra are included in Table 2. The calculated hyperfine coupling constants for the α -pyrrole, α -pyrroline, and *meso*-carbon atoms, as well as those for the pyrroline hydrogen atoms are generally larger than those derived from the simulations [e.g., $a(^{13}\text{C}^{6,16})$, 7.50 G (calculated) and 6.33 G (observed) and $a(^{1}\text{H}^{7,17})$, 9.26 G (calculated) and 6.75 G (observed)], whereas those for the nitrogen atoms are somewhat smaller [e.g., $a(^{14}\text{N}^{21,23})$, 0.93 G (calculated) and 1.30 (observed)]. Regardless, the relative magnitudes of the calculated hyperfine coupling constants for all of the distinct types of atoms in the complex parallel the observed values. The relative magnitudes of the hyperfine coupling constants for each of the atoms rendered symmetry inequivalent owing to the presence of the $\text{C}^{7,17}$ hydrogen atoms versus $\text{C}^{8,18}$ methyl groups are also consistent with the observed values [e.g., $a(^{13}\text{C}^{1,11})$, 5.73 (calculated), and 5.07 (observed); $a(^{13}\text{C}^{4,14})$, 5.60 (calculated), and 4.94 (observed)]. The calculations predict that the spin densities on the α -pyrrolic and α -pyrrolic carbon atoms are substantial, $\rho \sim 0.2$, as expected for the a_{1u} -like SOMO of bacteriochlorins.^{21,39} The calculations further predict that the spin densities on both the *meso*-carbon atoms and pyrrolic/pyrrolic nitrogen atoms are significant, $\rho \sim 0.1$ and $\rho \sim 0.05$ – 0.07 , respectively. This result contradicts the predictions of early calculations.²¹

Another noteworthy aspect of the calculations is the prediction that the hyperfine coupling constant of the *meso*-

hydrogen atoms ($\text{H}^{5,15}$ and $\text{H}^{10,20}$) is comparable to that of the pyrrolic hydrogen atoms ($\text{H}^{2,12}$ and $\text{H}^{3,13}$) and in the 1.0–1.1 G range. A second noteworthy aspect is the prediction that only one of the three hydrogens on each of the four methyl groups exhibits substantial hyperfine coupling (0.74 G versus 0.31 and 0.27 G; Figure 11; atom H' in Figure S2 of the Supporting Information). Consequently, one of the additional sets of four hydrogen atoms required for adequate spectral simulations is assigned to the *meso*-hydrogen atoms and the other additional set of four hydrogen atoms is assigned to the hydrogen atom on each methyl group with the largest calculated hyperfine coupling constant. These assignments will be investigated further in the future when the appropriate deuterated isotopomers of ZnBC are prepared.

IV. DISCUSSION

The spectroscopic studies of CuBC-NA and the isotopologues reported herein provide a detailed picture of the vibrational characteristics of the electronic ground state of the core bacteriochlorin macrocycle and how these vibrations are coupled to the lowest few singlet electronic excited states. Similarly, the studies of $[\text{ZnBC-NA}]^+$ and the isotopologues provide insights into the spin-density distributions in the π -cation radicals of bacteriochlorin macrocycles. We first address the vibrational and vibronic characteristics of the molecule and then turn to a discussion of the electron and spin densities in the HOMO/SOMO. In this discussion, we do not focus on the details of these physicochemical characteristics but rather on how these characteristics might influence processes in photosynthesis and artificial solar-energy conversion.

A. Vibrational and Vibronic Characteristics. The vibrational spectra, particularly the RR spectra, of CuBC are unremarkable with respect to the nature of the vibrational modes that are observed. In particular, the vibrations that exhibit intensity are primarily associated with bond stretches of the macrocycle, as is generally observed for all classes of tetrapyrrolic macrocycles.^{42,43} What is unusual is the extreme sparsity of the modes that undergo resonance enhancement in the Raman spectrum. The CuBC has 53 atoms and 153 normal modes. Excluding the peripheral methyl groups and hydrogen atoms, the 25-atom core of the macrocycle has 69 normal modes. Forty-seven of these modes are in-plane motions and of this group, 23 have A_g symmetry and might be expected to vibrationally couple to the electronic excited states, resulting in Raman intensity enhancements, yet only a few RR bands are observed. Indeed, for the Q_y state, the only mode with appreciable RR intensity is the 727 cm^{-1} accordion-like deformation. The absence of appreciable resonance-enhanced Raman activity leads to the view that the core macrocycle is extremely rigid and that the geometry differences between the ground and singlet excited electronic states are minimal. In the case of the Q_y state, this property is clearly visible in the characteristics of the absorption and fluorescence spectra, wherein the $Q_y(1,0)$ and $Q_y(0,1)$ vibronic satellites are dominated by a mode attributable to the accordion-like deformation (Figure 1 and Figure S1 of the Supporting Information). The rigidity of the macrocycle is also likely the origin of the small Stokes shift between the absorption and fluorescence spectra and the relatively narrow widths of the Q_y absorption bands.

The sparsity of the RR spectra of CuBC can be contrasted with the observations for other synthetic bacteriochlorins and natural bacteriochlorophylls. RR spectra have been previously

reported for the copper chelate of *meso*-tetraphenylbacteriochlorin and the nickel chelate of octaethylbacteriochlorin, as well as isotopologues of these molecules.^{22,23} The RR spectra of these complexes are more complex than those of CuBC. The RR spectra of the natural bacteriochlorophylls, both in solution and in proteins, are still more complex, exhibiting dozens of bands that span the low- and high-frequency regions of the RR spectra.^{44–50}

The RR spectra of other bacteriochlorin model complexes that have been studied differ from CuBC primarily in the nature and number of peripheral substituents on the macrocycle. Natural bacteriochlorophylls differ further in that the fifth, isocyclic ring is present (Chart 1). The natural chromophores also differ in that the central metal atom is magnesium not a transition metal. However, this difference is not a prime contributor to the increased complexity of the RR spectra of natural chromophores versus the model complexes, as is evidenced by the fact that a copper chelate of bacteriochlorophyll also exhibits complex RR spectra.⁴⁵ The picture that emerges is that both the peripheral substituents and isocyclic ring contribute to the increased spectral complexity. These effects are likely due to further symmetry lowering, which would render A_u -like vibrations RR active, and/or via the contribution of vibrations to the RR spectra that are primarily due to the substituents. In particular, modes due to the carbonyl groups on the isocyclic ring and acetyl substituent of bacteriochlorophyll *a* (Chart 1) are known to contribute to the RR spectra.^{42–44,46} In addition, vibrational assignments for the low-frequency modes of bacteriochlorophyll *a* indicate that many of the observed RR bands are due to substituent bending modes.⁴⁹ The isocyclic ring and acetyl carbonyl groups also conjugate with the π system of the macrocycle, and it is plausible that changes in electronic structure also result in increased vibronic activity.

A question that arises is whether the enhanced vibronic activity exhibited by natural bacteriochlorophylls is important for the primary processes of energy- and electron-transfer that drive photosynthesis. In this regard, time-resolved spectroscopic studies of reaction centers and antenna complexes have shown evidence of coherences that may be due to vibrational motions.^{51–62} Very recently, it has been shown that a particular vibrational mode near 685 cm^{-1} appears to couple the accessory bacteriochlorophylls and bacteriopheophytins in reaction centers.⁶² It might be speculated that this vibration in the natural chromophore is related to the accordion-like deformation of the core bacteriochlorin macrocycle. From a larger perspective, a key unanswered question is whether nature selected the bacteriochlorophyll molecule such that these coherences can occur and therefore drive the primary processes of photosynthesis or whether the coherences are unimportant and merely a natural consequence of the large number of vibrationally active modes of the natural chromophore. This question might be investigated by reconstituting native proteins (or suitable designer proteins) with synthetic bacteriochlorins, wherein the structural complexities of native bacteriochlorophylls are systematically added to the core macrocycle.

B. Electron- and Spin-Density Characteristics. The EPR spectra of $[\text{ZnBC-NA}]^+$ and the isotopologues exhibit many features in common with those previously reported for the π -cation radicals of the free base and zinc chelate of *meso*-tetraphenylbacteriochlorin and the zinc chelate of bacteriochlorophyll *a*, as well as various isotopologues of these species.^{20,21} Of particular note is the significant hyperfine

coupling constants observed for the hydrogen atoms ($\text{H}^{7,17}$) on the saturated, pyrroline rings. Early EPR studies attributed these large hyperfine couplings to spin-polarization effects arising from the presence of large spin densities on the α -carbon atoms ($\text{C}^{6,16}$; $\text{C}^{9,19}$) of the pyrroline rings in the A_{1u} -like SOMO of the bacteriochlorin macrocycle.²¹ The presence of large spin densities on the α -carbon atoms was not directly confirmed experimentally in these early studies but instead was based on molecular orbital calculations. The EPR studies reported herein on $[\text{ZnBC-}^{13}\text{C}^{6,16}]^+$ and $[\text{ZnBC-}^{13}\text{C}^{9,19}]^+$ provide direct evidence for the early prediction of the large spin densities on the α -pyrrolic carbon atoms. Likewise, the studies of $[\text{ZnBC-}^{13}\text{C}^{1,11}]^+$ and $[\text{ZnBC-}^{13}\text{C}^{4,14}]^+$ confirm the predicted large spin densities on the α -pyrrolic carbon atoms.

The early molecular-orbital calculation on the π -cation radicals of bacteriochlorins further predicted that the spin densities on the *meso*-carbon atoms (and nitrogen atoms) of the macrocycle are extremely small.²¹ If so, relatively small hyperfine coupling constants would be expected from the *meso*-carbon and nitrogen atoms, primarily arising from spin polarization effects due to the bonding of these atoms with the α -pyrrole and α -pyrroline carbon atoms. The relatively small ^{14}N nitrogen hyperfine couplings reported in early studies seemed qualitatively consistent with this view. The small ^{14}N hyperfine coupling constants are confirmed by the studies reported herein. However, contrary to the predictions of the early studies, the studies reported herein for $[\text{ZnBC-}^{13}\text{C}^{5,15}]^+$ and $[\text{ZnBC-}^{13}\text{C}^{10,20}]^+$ reveal quite large *meso*- ^{13}C hyperfine couplings. Such large couplings are too large to arise only from indirect spin polarization effects. Indeed, the DFT calculations reported herein indicate quite significant electron and spin densities on the *meso*-carbon atoms of the bacteriochlorin macrocycle (Figures 10 and 11; Table 2). The calculations also indicate substantial spin densities on the nitrogen atoms. Thus, the relatively small ^{14}N hyperfine coupling constants must result from a complex interplay of the spin density on these atoms with that on adjacent atoms.

The observation of significant electron and spin density on the *meso*-carbon atoms of the bacteriochlorin macrocycle has implications for the assembly of synthetic, bacteriochlorin-based light-harvesting arrays that contain covalent linkages between the constituent macrocycles. In this regard, our groups have previously shown in work on other types of tetrapyrrole-based arrays that the position of the covalent linker (β -pyrrole versus *meso*-carbon atom) can influence the rates of both excited-state energy transfer and ground-state hole transfer.¹⁵ In particular, the most rapid and efficient energy and/or electron/hole transfer would be promoted by connectivities at sites of large electron/spin density. The prevailing view that *meso*-carbon atoms of the HOMO/SOMO of bacteriochlorins did not exhibit significant electron/spin density prompted synthetic designs of arrays wherein the covalent linkage was confined to the β -pyrrole position, where significant electron/spin density was expected. The results reported herein showing that the *meso*-carbon atoms of bacteriochlorins do in fact exhibit significant electron/spin densities suggest that these positions may be well-suited for covalent linkages, thereby altering our thinking in synthetic design of multibacteriochlorin arrays.

■ ASSOCIATED CONTENT

📄 Supporting Information

Absorption and fluorescence spectra of ZnBC-NA; structure and complete atom numbering and labeling scheme for CuBC;

calculated bond lengths, bond angles, and $C^6-C^7-C^8-C^9$ torsional angles for **CuBC**, **ZnBC**, and **[ZnBC]⁺**; vibrational eigenvectors for the other observed modes of **CuBC**; $C_m(C_aNC_a)_{\text{pyrrole}}C_m$ accordion-like deformation animation; $C_m(C_aNC_a)_{\text{pyrroline}}C_m$ accordion-like deformation animation; complete ref 31. This material is available free of charge via the Internet at <http://pubs.acs.org>.

AUTHOR INFORMATION

Corresponding Authors

*E-mail: david.bocian@ucr.edu. Tel: 951-827-3660.

*E-mail: jlindsey@ncsu.edu. Tel: 919-515-6406.

*E-mail: holten@wustl.edu. Tel: 314-935-6502.

Notes

The authors declare no competing financial interest.

ACKNOWLEDGMENTS

This research was supported by grants from the Chemical Sciences, Geosciences and Biosciences Division, Office of Basic Energy Sciences, of the U.S. Department of Energy to D.F.B. (DE-FG02-05ER15660), J.S.L. (DE-FG02-96ER14632), and D.H. (DE-FG02-05ER15661).

REFERENCES

- (1) van Niel, C. B. Photosynthesis of Bacteria. *Cold Spring Harbor Symp. Quant. Biol.* **1935**, *3*, 138–150.
- (2) van Niel, C. B. The Culture, General Physiology, Morphology, and Classification of the Non-Sulfur Purple and Brown Bacteria. *Bacteriol. Rev.* **1944**, *8*, 1–118.
- (3) Golden, J. H.; Linstead, R. P.; Whitham, G. H. Chlorophyll and Related Compounds. Part VII. The Structure of Bacteriochlorophyll. *J. Chem. Soc.* **1958**, 1725–1732.
- (4) Fleming, I. The Absolute Configuration and the Structures of Chlorophyll and Bacteriochlorophyll. *J. Chem. Soc. C* **1968**, 2765–2770.
- (5) Brockmann, H., Jr.; Kleber, I. The Absolute Configuration of Bacteriochlorophyll-*a*. *Angew. Chem., Int. Ed.* **1969**, *8*, 610–611.
- (6) Blankenship, R. E. *Molecular Mechanisms of Photosynthesis*, 2nd ed.; Wiley-Blackwell: Hoboken, NJ, 2014.
- (7) Lee, H.; Cheng, Y.-C.; Fleming, G. R. Coherence Dynamics in Photosynthesis: Protein Protection of Excitonic Coherence. *Science* **2007**, *316*, 1462–1465.
- (8) Engel, G. S.; Calhoun, T. R.; Read, E. L.; Ahn, T.-K.; Mančal, T.; Cheng, Y.-C.; Blankenship, R. E.; Fleming, G. R. Evidence for Wavelike Energy Transfer Through Quantum Coherence in Photosynthetic Systems. *Nature* **2007**, *446*, 782–786.
- (9) Cheng, Y.-C.; Fleming, G. R. Dynamics of Light Harvesting in Photosynthesis. *Annu. Rev. Phys. Chem.* **2009**, *60*, 241–262.
- (10) Panitchayangkoon, G.; Hayes, D.; Fransted, K. A.; Caram, J. R.; Harel, E.; Wen, J.; Blankenship, R. E.; Engel, G. S. Long-Lived Quantum Coherence in Photosynthetic Complexes at Physiological Temperature. *Proc. Natl. Acad. Sci. U. S. A.* **2010**, *107*, 12766–12770.
- (11) Ishizaki, A.; Fleming, G. R. Quantum Coherence in Photosynthetic Light Harvesting. *Annu. Rev. Condens. Matter Phys.* **2012**, *3*, 333–361.
- (12) Smyth, C.; Fassioli, F.; Scholes, G. D. Measures and Implications of Electronic Coherence in Photosynthetic Light-Harvesting. *Philos. Trans. R. Soc., A* **2012**, *370*, 3728–3749.
- (13) Ana, J. M.; Scholes, G. D.; van Grondelle, R. A Little Coherence in Photosynthetic Light Harvesting. *Bioscience* **2010**, *109*, 1093/biosci/bit002.
- (14) Scholes, G. D.; Smyth, C. Perspective: Detecting and Measuring Exciton Delocalization in Photosynthetic Light Harvesting. *J. Chem. Phys.* **2014**, *140*, 110901-1–110901-8.
- (15) Holten, D.; Bocian, D. F.; Lindsey, J. S. Probing Electronic Communication in Covalently Linked Multiporphyrin Arrays. A Guide to the Rational Design of Molecular Photonic Devices. *Acc. Chem. Res.* **2002**, *35*, 57–69.
- (16) Lindsey, J. S.; Mass, O.; Chen, C.-Y. Tapping the Near-Infrared Spectral Region with Bacteriochlorin Arrays. *New J. Chem.* **2011**, *35*, 511–516.
- (17) Yang, E.; Wang, J.; Diers, J. R.; Niedzwiedzki, D. M.; Kirmaier, C.; Bocian, D. F.; Lindsey, J. S.; Holten, D. Probing Electronic Communication for Efficient Light-Harvesting Functionality: Dyads Containing a Common Perylene and a Porphyrin, Chlorin, or Bacteriochlorin. *J. Phys. Chem. B* **2014**, *118*, 1630–1647.
- (18) Goedheer, J. C. Investigations on Bacteriochlorophyll in Organic Solutions. *Biochim. Biophys. Acta* **1958**, *27*, 478–490.
- (19) Eimhjellen, K. E.; Aasmundrud, O.; Jensen, A. A New Bacterial Chlorophyll. *Biochem. Biophys. Res. Commun.* **1963**, *10*, 232–236.
- (20) Fajer, J.; Borg, D. C.; Forman, A.; Felton, R. H.; Dolphin, D.; Vegh, L. The Cation Radicals of Free Base and Zinc Bacteriochlorin, Bacteriochlorophyll, and Bacteriopheophytin. *Proc. Natl. Acad. Sci. U.S.A.* **1974**, *71*, 994–998.
- (21) Fajer, J.; Davis, M. S. Electron Spin Resonance of Porphyrin π Cations and Anions. In *The Porphyrins*, Dolphin, D., Ed.; Academic Press: New York, 1979; Vol. 4, pp 197–256.
- (22) Donohoe, R. J.; Atamian, M.; Bocian, D. F. Resonance Raman Spectra and Normal-Coordinate Analysis of Reduced Porphyrins. 2. Copper(II) Tetraphenylchlorin and Copper (II) Tetraphenylbacteriochlorin. *J. Phys. Chem.* **1989**, *93*, 2244–2252.
- (23) Hu, S.; Mukherjee, A.; Spiro, T. G. Synthesis, Vibrational Spectra, and Normal Mode Analysis of Nickel(II) 1,5-Dihydroxy-1,5-dimethyloctaethylbacteriochlorin: A Model for Bacteriochlorophylls. *J. Am. Chem. Soc.* **1993**, *115*, 12366–12377.
- (24) Lin, C.-Y.; Spiro, T. G. Resonance Raman, Infrared, and Normal Coordinate Analysis of Free-Base Tetraphenylbacteriochlorin: A Model for Bacteriopheophytins. *J. Phys. Chem. B* **1997**, *101*, 472–482.
- (25) Lin, C.-Y.; Blackwood, M. E., Jr.; Kumble, R.; Hu, S.; Spiro, T. G. Structural Changes for π -Radicals of Free-Base Tetraphenylbacteriochlorin: A Model for the Electron Donor and Acceptor in Bacterial Reaction Centers. *J. Phys. Chem. B* **1997**, *101*, 2372–2380.
- (26) Chen, C.-Y.; Bocian, D. F.; Lindsey, J. S. Synthesis of 24 Bacteriochlorin Isotopologues, Each Containing a Symmetrical Pair of ^{13}C or ^{15}N Atoms in the Inner Core of the Macrocyclic. *J. Org. Chem.* **2014**, *79*, 1001–1016.
- (27) Chen, C.-Y.; Taniguchi, M.; Lindsey, J. S. NMR Spectral Properties of 16 Synthetic Bacteriochlorins with Site-Specific ^{13}C or ^{15}N Substitution. *J. Porphyrins Phthalocyanines* **2014**, *18*, 10.1142/S1088424614500199.
- (28) Carter, D. A.; Thompson, W. R.; Taylor, C. E.; Pemberton, J. E. Frequency/Wavelength Calibration of Multipurpose Multichannel Raman Spectrometers. Part II: Calibration Fit Considerations and Calibration Standards. *Appl. Spectrosc.* **1995**, *49*, 1561–1576.
- (29) Yu, N.-T.; Srivastav, R. B. Resonance Raman Spectroscopy of Heme Proteins with Intensified Vidicon Detectors: Studies of Low Frequency Modes and Excitation Profiles in Cytochrome *c* and Hemoglobin. *J. Raman Spectrosc.* **1980**, *9*, 166–171.
- (30) Duling, J. R. Simulation of Multiple Isotropic Spin-Trap EPR Spectra. *J. Magn. Reson., Ser. B* **1994**, *104*, 105–110, <http://www.niehs.nih.gov/research/resources/software/tools/index.cfm>, (accessed March 18, 2010).
- (31) Frisch, M. J.; Trucks, G. W.; Schlegel, H. B.; Scuseria, G. E.; Robb, M. A.; Cheeseman, J. R.; Scalmani, G.; Barone, V.; Mennucci, B.; Petersson, G. A.; et al. *Gaussian 09*, revision D.01; Gaussian, Inc.: Wallingford, CT, 2009.
- (32) Dennington, R.; Keith, T.; Millam, J. *GaussView*, version 5; Semichem Inc.: Shawnee Mission, KS, 2009.
- (33) Jamróz, M. H. Vibrational Energy Distribution Analysis (VEDA): Scopes and Limitations. *Spectrochim. Acta, Part A* **2013**, *114*, 220–230, <http://www.smmg.pl/index.php/software/sowtware-vedahtml>, (accessed Sept 5, 2013).
- (34) Hedegård, E. D.; Kongsted, J.; Sauer, S. P. A. Optimized Basis Sets for Calculation of Electron Paramagnetic Resonance Hyperfine

Coupling Constants: aug-cc-pVTZ-J for the 3d Atoms Sc–Zn. *J. Chem. Theory Comput.* **2011**, *7*, 4077–4087.

(35) Feller, D. The Role of Databases in Support of Computational Chemistry Calculations. *J. Comput. Chem.* **1996**, *17*, 1571–1586.

(36) Schuchardt, K. L.; Didier, B. T.; Elsethagen, T.; Sun, L.; Gurumoorathi, V.; Chase, J.; Li, J.; Windus, T. L. Basis Set Exchange: A Community Database for Computational Sciences. *J. Chem. Inf. Model.* **2007**, *47*, 1045–1052, <https://BSE.pnl.gov/bse/portal>, (accessed May 22, 2013).

(37) Yang, E.; Kirmaier, C.; Krayner, M.; Taniguchi, M.; Kim, H.-J.; Diers, J. R.; Bocian, D. F.; Lindsey, J. S.; Holten, D. Photophysical Properties and Electronic Structure of Stable, Tunable, Synthetic Bacteriochlorins: Extending the Features of Native Photosynthetic Pigments. *J. Phys. Chem. B* **2011**, *115*, 10801–10816.

(38) Chen, C.-Y.; Sun, E.; Fan, D.; Taniguchi, M.; McDowell, B. E.; Yang, E.; Diers, J. R.; Bocian, D. F.; Holten, D.; Lindsey, J. S. Synthesis and Photophysical Properties of Metallobacteriochlorins. *Inorg. Chem.* **2012**, *51*, 9443–9464.

(39) Gouterman, M. Optical Spectra and Electronic Structure of Porphyrins and Related Rings. In *The Porphyrins*; Dolphin, D., Ed.; Academic Press: New York, 1978; Vol. 3, pp 1–165.

(40) Kobayashi, M.; Akiyama, M.; Kano, H.; Kise, H. Spectroscopy and Structure Determination. In *Chlorophylls and Bacteriochlorophylls: Biochemistry, Biophysics, Functions and Applications*; Grimm, B.; Porra, R. J.; Rüdiger, W.; Scheer, H., Eds.; Springer: Dordrecht, The Netherlands, 2006; pp 79–94.

(41) Wertz, J. E.; Bolton, J. R. Electron Spin Resonance. Elementary Theory and Practical Applications. McGraw-Hill: New York, 1972.

(42) Schick, G. A.; Bocian, D. F. Resonance Raman Studies of Hydroporphyrins and Chlorophylls. *Biochim. Biophys. Acta* **1987**, *895*, 127–154.

(43) Procyk, A. D.; Bocian, D. F. Vibrational Characteristics of Tetrapyrrolic Macrocycles. *Annu. Rev. Phys. Chem.* **1992**, *43*, 465–496.

(44) Lutz, M.; Robert, B. Chlorophylls and the Photosynthetic Membrane. In *Biological Applications of Raman Spectroscopy*; Spiro, T. G., Ed.; Wiley: New York, 1988; Vol. 3, pp 347–411.

(45) Donohoe, R. J.; Frank, H. A.; Bocian, D. F. Resonance Raman Spectra and Normal Mode Descriptions of a Bacteriochlorophyll *a* Model Complex. *Photochem. Photobiol.* **1988**, *48*, 531–537.

(46) Palaniappan, V.; Martin, P. C.; Chynwat, V.; Frank, H. A.; Bocian, D. F. Comprehensive Resonance Raman Study of Photosynthetic Reaction Centers from *Rhodobacter sphaeroides*. Implications for Pigment Structure and Pigment–Protein Interactions. *J. Am. Chem. Soc.* **1993**, *115*, 12035–12049.

(47) Cherepy, N. J.; Shreve, A. P.; Moore, L. J.; Franzen, S.; Boxer, S. G.; Mathies, R. A. Near-Infrared Resonance Raman Spectroscopy of the Special Pair and the Accessory Bacteriochlorophylls in Photosynthetic Reaction Centers. *J. Phys. Chem.* **1994**, *98*, 6023–6029.

(48) Diers, J. R.; Bocian, D. F. Q_y-Excitation Resonance Raman Spectra of Bacteriochlorophyll Observed under Fluorescence-Free Conditions. Implications for Cofactor Structure in Photosynthetic Proteins. *J. Am. Chem. Soc.* **1995**, *117*, 6629–6630.

(49) Czarnecki, K.; Diers, J. R.; Chynwat, V.; Erickson, J. P.; Frank, H. A.; Bocian, D. F. Characterization of the Strongly Coupled, Low-Frequency Vibrational Modes of the Special Pair of Photosynthetic Reaction Centers via Isotopic Labeling of the Cofactors. *J. Am. Chem. Soc.* **1997**, *119*, 415–426.

(50) Cherepy, N. J.; Shreve, A. P.; Moore, L. J.; Boxer, S. G.; Mathies, R. A. Electronic and Nuclear Dynamics of the Accessory Bacteriochlorophylls in Photosynthetic Reaction Centers from Resonance Raman Intensities. *J. Phys. Chem. B* **1997**, *101*, 3250–3260.

(51) Vos, M. H.; Lamry, J.-C.; Robles, S. J.; Youvan, D. C.; Breton, J.; Martin, J.-L. Direct Observation of Vibrational Coherence in Bacterial Reaction Centers Using Femtosecond Absorption Spectroscopy. *Proc. Natl. Acad. Sci. U.S.A.* **1991**, *88*, 8885–8889.

(52) Vos, M. H.; Rappaport, F.; Lambry, J.-C.; Breton, J.-L.; Martin, J.-L. Visualization of Coherent Nuclear Motion in a Membrane Protein by Femtosecond Spectroscopy. *Nature* **1993**, *363*, 320–325.

(53) Vos, M. H.; Jones, M. R.; Hunter, C. N.; Breton, J.; Lambry, J.-C.; Martin, J.-L. Coherent Dynamics During the Primary Electron-Transfer Reaction in Membrane-Bound Reaction Centers of *Rhodobacter sphaeroides*. *Biochemistry* **1994**, *33*, 6750–6757.

(54) Vos, M. H.; Jones, M. R.; Hunter, C. N.; Breton, J.; Martin, J.-L. Coherent Nuclear Dynamics at Room Temperature in Bacterial Reaction Centers. *Proc. Natl. Acad. Sci. U.S.A.* **1994**, *91*, 12701–12705.

(55) Christensson, N.; Kauffmann, H. F.; Pullerits, T.; Mančal, T. Origin of Long-lived Coherences in Light-Harvesting Complexes. *J. Phys. Chem. B* **2012**, *116*, 7449–7454.

(56) Huo, P.; Coker, D. F. Influence of Environment Induced Correlated Fluctuations in Electronic Coupling on Coherent Excitation Energy Transfer Dynamics in Model Photosynthetic Systems. *J. Chem. Phys.* **2012**, *136*, 115102-1–115102-17.

(57) Kim, H. W.; Kelly, A.; Park, J. W.; Rhee, Y. M. All-Atom Semiclassical Dynamics Study of Quantum Coherence in Photosynthetic Fenna–Matthews–Olson Complex. *J. Am. Chem. Soc.* **2012**, *134*, 11640–11651.

(58) Richards, G. H.; Wilk, K. E.; Curmi, P. M. G.; Quiney, H. M.; Davis, J. A. Coherent Vibronic Coupling in Light-Harvesting Complexes from Photosynthetic Marine Algae. *J. Phys. Chem. Lett.* **2012**, *3*, 272–277.

(59) Tiwari, V.; Peters, W. K.; Jonas, D. M. Electronic Resonance with Anticorrelated Pigment Vibrations Drives Photosynthetic Energy Transfer Outside the Adiabatic Framework. *Proc. Natl. Acad. Sci. U.S.A.* **2013**, *110*, 1203–1208.

(60) Chin, A. W.; Prior, J.; Rosenbach, R.; Caycedo-Soler, F.; Huelga, S. F.; Plenio, M. B. The Role of Non-Equilibrium Vibrational Structures in Electronic Coherence and Recoherence in Pigment–Protein Complexes. *Nat. Phys.* **2013**, *9*, 113–118.

(61) Chenu, A.; Christensson, N.; Kauffmann, H. F.; Mančal, T. Enhancement of Vibronic and Ground-state Vibrational Coherences in 2D Spectra of Photosynthetic Complexes. *Sci. Rep.* **2013**, *3*, 2029.

(62) Ryu, I. S.; Dong, H.; Fleming, G. R. Role of Electronic-Vibrational Mixing in Enhancing Vibrational Coherence in the Ground Electronic States of Photosynthetic Bacterial Reaction Center. *J. Phys. Chem. B* **2014**, *118*, 1381–1388.